Microfluidics and Nanofluidics (2018) 22:96
https://doi.org/10.1007/s10404-018-2119-4

RESEARCH PAPER

Characterization of electrowetting, contact angle hysteresis, and adhesion on digital microfluidic devices with inkjet-printed electrodes

Kimberly A. Bernetski[1] · Collin T. Burkhart[1] · Kara L. Maki[2] · Michael J. Schertzer[1]

Received: 29 March 2018 / Accepted: 17 August 2018 / Published online: 22 August 2018

Abstract

This investigation characterizes electrowetting performance, contact angle hysteresis, contact line pinning force, and adhesion work on digital microfluidic devices with inkjet-printed electrodes. It also demonstrates electrowetting-induced droplet detachment on these devices. Average performance was similar to cleanroom-fabricated devices in all experimental measurements, but variability was persistently higher on inkjet-printed devices. This appears to be consistent with increased defect density and variation in local electrowetting number caused by increased roughness of printed electrodes. This work suggests that inkjet-printed devices are suitable for the study of colloidal transport and deposition under electric fields and electrowetting-induced droplet detachment when accompanied by rigorous uncertainty analysis.

Keywords Digital microfluidics · Electrowetting on dielectric · Inkjet printing · Contact angle hysteresis · Electrowetting-assisted droplet detachment

Abbreviations

A	Subscript denoting a property when the contact line is advancing
C_H	Helmholtz capacitance per unit area of the solid–liquid interface
Ew	Electrowetting number, a ratio of electrical and interfacial energy at the solid–liquid interface and subscript denoting a property under that electrowetting number
PTFE	Subscript denoting a property associated with PTFE (Teflon AF)
R	Subscript denoting a property when the contact line is receding
SU-8	Subscript denoting a property associated with SU-8 3005
tot	Subscript denoting the sum of all components of a parameter
U	Root mean squared voltage and subscript denoting a property under that voltage
W_{adh}	Adhesion work
γ	Surface tension between the liquid and surrounding medium
δ	Uncertainty (2 standard deviations) in a given experimental parameter
δF	Contact line pinning force
ε_0	Permittivity of free space
ε	Relative permittivity
θ	Contact angle
0	Subscript denoting the initial unactuated contact angle

Electronic supplementary material The online version of this article (https://doi.org/10.1007/s10404-018-2119-4) contains supplementary material, which is available to authorized users.

✉ Michael J. Schertzer
mjseme@rit.edu

Kimberly A. Bernetski
Kab3322@rit.edu

Collin T. Burkhart
ctb6973@rit.edu

Kara L. Maki
kmaki@rit.edu

[1] Mechanical Engineering, Rochester Institute of Technology, 76 Lomb Memorial Drive, Rochester, NY 14623, USA

[2] School of Mathematical Sciences, Rochester Institute of Technology, 85 Lomb Memorial Drive, Rochester, NY 14623, USA

1 Introduction

Digital microfluidic (DMF) devices manipulate fluid interfaces of confined and unconfined droplets through the application of electric fields (Cho et al. 2003; Paik et al. 2003; Mugele and Baret 2005; Eral et al. 2011; Mampallil et al. 2012; Nelson and Kim 2012; Choi et al. 2012; Orejon et al. 2013; Samiei et al. 2016). These devices leverage the electrowetting on dielectric (EWOD) effect to reduce the apparent contact angle between the droplet and a dielectric material above an active electrode. For low-to-moderate voltages, this behavior is described by the Young–Lippmann (or electrowetting) equation

$$\cos\left(\theta_{\mathrm{U}}\right) = \cos\left(\theta_0\right) + \left(C_{\mathrm{H}}U^2\right)/2\gamma = cos\theta_0 + \mathrm{Ew}, \qquad (1)$$

here C_{H} is the Helmholtz capacitance per unit area of the solid–liquid interface, U is the root-mean-squared (RMS) voltage, γ is the surface tension between the liquid and the surrounding medium, θ_0 is the initial unactuated contact angle, and θ_{U} is the apparent contact angle observed at a given RMS voltage. The change in the interface shape depends on the electrowetting number (Ew), a ratio of electrical and interfacial energy at the solid–liquid interface (Nelson and Kim 2012). Electrowetting always reduces the contact angle since Ew is dependent on U^2. Electrowetting behavior is well predicted by (1) low-to-moderate voltages, but the prediction breaks down above a system-dependent voltage where the contact angle becomes saturated (Walker and Shapiro 2006; Mugele 2009; Klarman et al. 2011; Nelson and Kim 2012). Comprehensive reviews of these devices and their applications are provided by Mugele and Baret (2005), Nelson and Kim (2012), Choi et al. (2012), and Wang et al. (2017).

While DMF devices can be used in a variety of biological applications (Choi et al. 2012), they have yet to achieve a high level of commercial success due in part to the expense related to microfabrication techniques. One of the advantages of DMF devices is that they do not require channels, pumps, or valves like many other microfluidic technologies. However, these devices are primarily fabricated using cleanroom facilities. This makes them significantly more expensive to produce than commercially successful paper microfluidic devices, such as lateral flow pregnancy testing assays (Dixon et al. 2016).

Attempts to reduce fabrication costs of DMF devices typically focus on alternate techniques to create conductive electrodes or deposit dielectric and hydrophobic polymer layers (Watson et al. 2006; Abdelgawad and Wheeler 2007; Ko et al. 2014; Fobel et al. 2014; Dixon et al. 2016; Samiei et al. 2016; Wang et al. 2017). Low-cost techniques for creating electrodes on these devices outside a cleanroom include: microcontact printing (Watson et al. 2006), laser printing on printed circuit boards (Abdelgawad and Wheeler 2007), patterning with hand-drawn photomasks (Abdelgawad and Wheeler 2007), and inkjet printing (Ko et al. 2014; Fobel et al. 2014; Dixon et al. 2016). While each technique reduces fabrication costs, inkjet printing offers an attractive combination of affordability, accessibility, feature resolution, and repeatability. For example, Dixon et al. reported material costs of $0.63 per device using an Epson C88 + inkjet printer ($120) and commercially available conductive ink that could print electrodes on DMF devices with a resolution on the order of 60 μm (Dixon et al. 2016).

Various methods for fabrication of dielectric and polymer films on DMF devices also provide different advantages and disadvantages. These polymer layers can be added by spin coating (Watson et al. 2006; Ko et al. 2014; Fobel et al. 2014), roll-to-roll coating (Dixon et al. 2016), and manual application of household plastic wrap (Abdelgawad and Wheeler 2007). While application of plastic wrap offers the lowest cost solution, resultant droplet motion was sluggish (Abdelgawad and Wheeler 2007). Conversely, droplet velocities were similar to cleanroom-fabricated devices when polymer films were deposited using spin and roll-to-roll coating (Watson et al. 2006; Ko et al. 2014; Fobel et al. 2014; Dixon et al. 2016). Spin-coating fabrication offers the advantage of low equipment costs (~$5000), while roll-to-roll coating offers higher maximum throughput at a significantly larger capital expense (~$100,000).

The effectiveness of the alternate fabrication techniques described above has been generally characterized by comparing the velocity of confined droplets on low-cost and cleanroom-fabricated devices (Watson et al. 2006; Abdelgawad and Wheeler 2007; Ko et al. 2014; Fobel et al. 2014; Dixon et al. 2016). Velocity measurements in these works demonstrate that DMF devices with inkjet-printed electrodes are suitable for lab on a chip (LOC) applications that manipulate confined droplets to automate biological protocols. While droplet velocity is critically important in many DMF LOC applications, different parameters play more important role in other DMF applications (Eral et al. 2011; Lee et al. 2012, 2014; Mampallil et al. 2012; Hong et al. 2013, 2015; Orejon et al. 2013; Mu et al. 2014; Chae et al. 2015). For example, control of colloidal transport and deposition in evaporating droplets with electric fields is strongly dependent on contact angle hysteresis and pinning force at the contact line (Eral et al. 2011; Mampallil et al. 2012; Orejon et al. 2013; Mu et al. 2014), and the use of electrowetting-induced droplet detachment to shed fluid from working surfaces is dependent on adhesion work at the interface between the droplet and the substrate (Lee et al. 2012, 2014; Hong et al. 2013, 2015; Chae et al. 2015). While droplet velocity is a function of electrowetting actuation and contact angle hysteresis (Schertzer et al. 2010), mobile droplets in DMF devices have an actuated advancing contact line and an unactuated receding contact line. The role of hysteresis may be different

in evaporating droplets with consistently receding actuated contact lines. Furthermore, observing comparable velocities on inkjet-printed and cleanroom-fabricated devices does not necessarily demonstrate that this fabrication technique is suitable for electrowetting-induced droplet detachment as adhesion work is not an explicit function of droplet velocity. Since hysteresis and adhesion work have not been explicitly characterized on devices with inkjet-printed electrodes, it is not yet clear if this fabrication method is suitable for these types of investigations.

This investigation compares electrowetting behavior, contact angle hysteresis, contact line pinning force, and adhesion energy of unconfined droplets on DMF devices with inkjet-printed and cleanroom-fabricated electrodes. This information is used to evaluate the effectiveness of inkjet-printed DMF devices for applications of colloidal transport and deposition in evaporating droplets under applied electric fields and electrowetting-induced droplet detachment. If this fabrication technique is suitable for these applications, the reduction in cost will help make studies in these areas more accessible and enable impactful work in a wide variety of applications including: fluid handling in biomedical applications (McHale 2007; Ragoonanan and Aksan 2008; Lee et al. 2012; Trantum et al. 2012; Wen et al. 2013; Gulka et al. 2014; Chae et al. 2015; Hong et al. 2015), fabrication of flexible electronics (Layani et al. 2009; Bromberg et al. 2013a, b), nanoparticle self-assembly (Chen et al. 1999; Orejon et al. 2011; Bellido et al. 2012; Saha et al. 2012; Corkidi et al. 2016), fabrication of liquid lenses (Kuiper and Hendriks 2004; Kong et al. 2017), and electrowetting displays (Hayes and Feenstra 2003; Roghair et al. 2015), and active removal of droplets from windshields, condensers, and fuel cells (Kim 2004; Palan and Shepard 2006; Kim and Kaviany 2007, 2010; Mannetje et al. 2011).

2 Experimental methodology

2.1 Device fabrication

The experimental facility used in this investigation consisted of a digital microfluidic device, an imaging system, a dispensed droplet, and an actuation system. Devices in this investigation are referred to as cleanroom-fabricated devices (CRFs) (Fig. 1a) or inkjet-printed devices (IJPs) (Fig. 1b) depending on how the conductive layer of the device was deposited. While the fabrication method of the conductive layer differed, both device types consisted of a single unpatterned electrode (Fig. 1).

The conductive layer on CRFs was created in the Semiconductor and Microsystems Fabrication Laboratory (SMFL) cleanroom at RIT. The device substrate (Corning plain glass slide, 50 mm × 75 mm) was cleaned in piranha

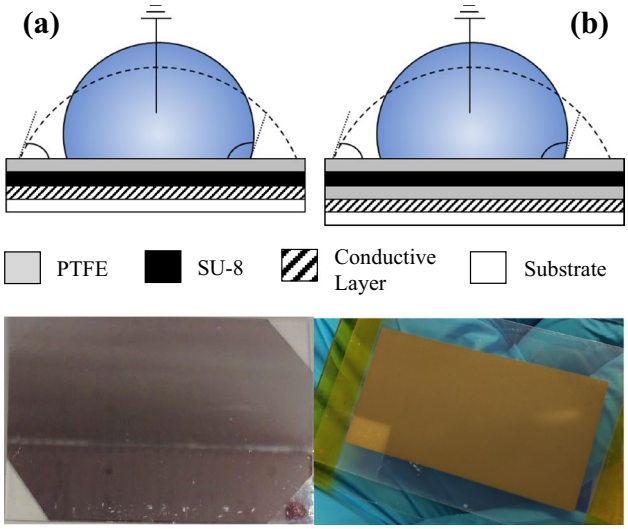

Fig. 1 Side-view sketches and top-view images of **a** cleanroom-fabricated (CRF) and **b** inkjet-printed (IJP) devices

organic solvent, then sputter coated with aluminum (~1 µm). Dielectric (SU-8 3005 ~6.4 µm) films were deposited using a two-stage spin-coating process (500 rpm for 10 s; 4000 rpm for 30 s; acceleration of 300 rpm/s between stages). Devices were then soft baked (Fisher Scientific Isotemp) for two and a half minutes at 95 °C, cured in an Electro-Lite EC-500 (365 nm for 30 s), and hard baked for three minutes at 150 °C. Finally, hydrophobic films of polytetrafluoroethylene (PTFE Teflon AF ~100 nm) were spun onto devices at 2000 rpm for 1 min and hard baked at 160 °C for 10 min.

While dielectric layers used in this investigation are thicker than the 1–2 µm layer Parylene-C films that are often deposited by chemical vapor deposition (CVD) in multiple DMF lab-on-a-chip investigations (i.e., Schertzer et al. 2012), they are consistent with investigations examining low-cost fabrication techniques. For example, Dixon et al. used 5–16 µm roll-coated Cyanoresin CR-S cyanoethyl pullulan films (Dixon et al. 2016) and typical spin-coated DMF dielectric layers include 6 µm PDMS (Watson et al. 2006) and 5–12 µm SU-8 films (Torabinia et al. 2018; Wang et al. 2018). The thickness of the films used here is also similar to several recent DMF investigations examining biomedical applications (Rackus et al. 2017; Ng et al. 2018) and electrowetting-induced droplet detachment (Lee et al. 2014; Hong et al. 2015; Cavalli et al. 2016) that use CVD to deposit 2.5–7 µm Parylene-C dielectric layers to reduce the risk of dielectric breakdown.

Electrodes on IJPs were deposited in a manner similar to that described by Dixon et al. (Dixon et al. 2016). An Epson Stylus C88 + color inkjet printer was loaded with cartridges of silver nanoink (Novacentrix JS-B25P) in the black, cyan, and magenta nozzles; the yellow nozzle was loaded using yellow ink. The conductive layer was printed on a flexible

polyethylene terephthalate (PET) film (Novacentrix Novele print media) using print settings as shown in Table 1. Conductive layers were cured at room temperature overnight before deposition of dielectric and hydrophobic layers unless otherwise indicated.

After electrode curing, IJPs were cut out of the printed sheet and mounted on glass slides using adhesive polyimide tape. Like the CRFs, first-generation devices were subsequently coated with SU-8 and PTFE by spin coating outside the cleanroom. Unfortunately, it was found that these devices were unstable as the SU-8 film did not bond well to the print media. To remedy this issue, a ~100 nm layer of PTFE was deposited on the media on all IJPs after printing and prior to SU-8 deposition. Despite being deposited using the same spin-coating parameters, SU-8 layers deposited on top of this insulating PTFE were thinner (~4.4 µm) than those on CRFs (~6.4 µm). This result is consistent with previous works that demonstrate that spin-coating photoresist on fluoropolymers can be difficult due to high hydrophobicity (Li et al. 2011; Ikawa et al. 2012; Zhang et al. 2017). While adhesion promoters can be used to improve results, photoresists with viscosities above approximately 50 *cst* can be deposited directly (Li et al. 2011). The manufacturer-reported viscosity of SU-8 3005 is 65 *cst*. The combination of moderate viscosity of the photoresist and low surface energy of the PTFE film appears to combine to reduce the thickness of the spin-coated SU-8 film.

Since the difference in the dielectric layer thickness on IJP and CRF devices creates a difference in the capacitance per unit area of the device types used in this investigation, performance is generally compared as a function of electrowetting number (Ew) and not applied voltage (U). Electrowetting numbers on both device types were determined using the surface tension between the water and the surrounding air ($\gamma = 72.8$ mN/m), the permittivity of free space ($\varepsilon_0 = 8.85$ pF/m), and the thickness and relative permittivity of SU-8 ($\varepsilon_{SU\text{-}8} = 3.2[-]$) and PTFE ($\varepsilon_{PTFE} = 2.0[-]$).

To improve the longevity of the print heads, the dead volume of ink in the printer was purged at the end of each printing session using a diluted cleaning solution. Stock cleaning solution consisted of glycerin, ammonia (~1 M), and isopropyl alcohol in a 1:2:10 ratio. The stock solution was diluted with three parts deionized water per one part cleaning solution prior to use. The diluted solution was loaded into each nozzle and used to print a repeated pattern of squares until the resulting prints were damp with cleaning solution and no ink was visible.

Table 1 Inkjet printer settings

Parameter	Setting
Quality	Best photo
Paper	Ultra-glossy
Print	High speed off

2.2 Device operation

Droplets were actuated using a 1 kHz AC signal produced by an NI PXI-5402 signal generator that was amplified up to 200 V_{RMS} using a Trek PZD700A amplifier. This signal was applied to the bond pad on the device and continuously monitored using an NI PXI-4072 digital multimeter. Droplets were grounded using one of the two methods. When generating electrowetting curves, a 22-nm diameter tungsten wire was inserted into a droplet of fixed volume. When measuring contact angle hysteresis, the metallic tip of a Ramé–Hart microdispenser within the droplet was grounded. This allowed for actuation of the droplet while adding or removing fluid.

Device quality was characterized by measuring surface roughness, electrowetting performance, and the advancing and receding contact angles for voltages from 0 to 200 V_{RMS}. Surface roughness was measured using a Nanovea ST400 profilometer.

Electrowetting performance was examined by measuring the apparent contact angle as a function of applied voltage. Deionized (DI) water droplets (3 µL) were deposited above the large unpatterned conductive layer on each device type using a micropipette before being grounded. Care was taken to ensure that measurement sites were not reused to eliminate any effects of fouling on the surface from previous tests. Devices were placed on the backlit stage of a Ramé–Hart model 250 goniometer where side-view images were captured at a rate of 10 frames per second (fps). DROPimage Advanced software was used to measure droplet width and mean contact angle for each frame.

Contact angle hysteresis as a function of applied voltage was measured using a similar procedure. Here, a Ramé–Hart microdispenser with a grounded metallic syringe tip was used to gradually add or remove fluid from a droplet until the contact line began to move. The advancing and receding contact angles reported here are the mean angles measured by the Ramé–Hart DROPimage software while the contact line was advancing or receding (Fig. 2).

Electrowetting-induced droplet detachment experiments were performed on both device types using 5 µL droplets of salt solution (~1 mM NaCl) grounded by tungsten wire. Droplets were actuated with a sequence of square wave pulses tuned to a wetting time of approximately 7 ms (Hong et al. 2013). Side-view images of the droplet response were captured in the DROPimage software at 40 fps.

All measurements reported here were repeated at least three times and error bars on related figures represent two standard deviations (95% confidence interval).

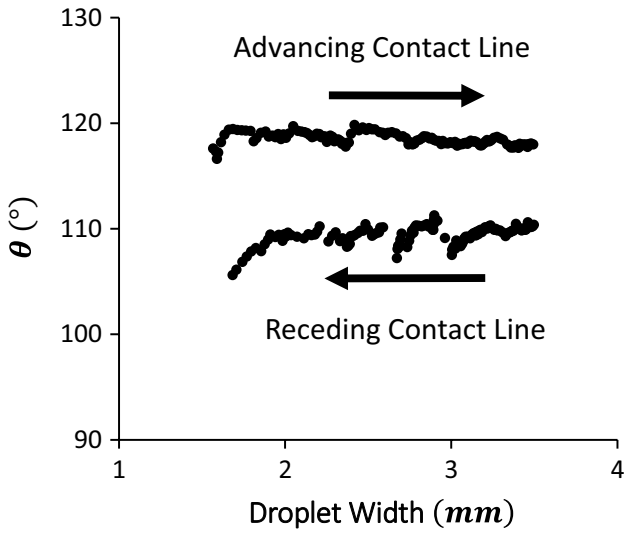

Fig. 2 Typical example of raw data used to determine advancing (θ_A) and receding (θ_R) contact angles

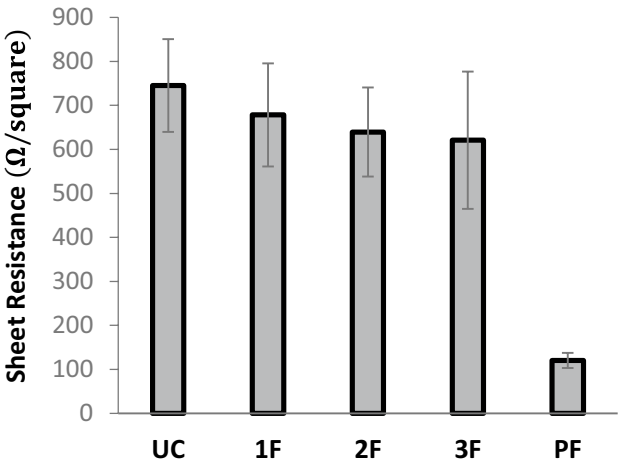

Fig. 3 Sheet resistance of bare IJP electrodes with the following treatments methods: uncured (UC), exposure to one (1F), two (2F), and three flashes (3F), and PulseForge sintering (PF)

3 Results and discussion

Inkjet-printed electrodes were not actively sintered in this investigation. Instead, they were allowed to cure at room temperature overnight as in Dixon et al. (2016). The suitability of this protocol was tested by examining the conductivity of the printed features using this passive technique and two active methods of reducing sheet resistance of inkjet-printed electrodes. The first was a low-cost method similar to that reported by Yung et al. (2010) where electrodes were subjected to multiple exposures from a DSLR camera flash (Nikon Speedlight DB-600). The second was photosintering in a Novacentrix PulseForge 3300. PulseForge processing requires a large capital investment (~ $1 M) but allows for rapid photosintering of inkjet-printed conductive electrodes.

Electrodes that were passively cured had a sheet resistance of 745 ± 105 mΩ/square (Fig. 3). Camera flash exposure reduced resistivity, but diminishing returns were observed with multiple exposures. The maximum reduction in resistivity was approximately 17% after three exposures. This was consistent with results reported by Yung et al. (2010). As expected, the improvement in resistivity with the PulseForge (~ 84%) was far superior to that of the low-cost camera flash method. While both curing methods reduced electrode resistivity, neither was adopted in this investigation. The benefit of reduced resistivity in electrowetting applications is likely small as the current in the devices is negligible. Furthermore, both methods to improve resistivity represent an increase in cost and processing time for the devices. While these methods were not implemented in this investigation, they may be attractive for commercial application of these devices.

Surface roughness of inkjet-printed electrodes was examined to determine if it would have a significant impact on the hydrophobicity and contact line dynamics on the device. The RMS roughness of the printed electrodes across three separate devices was found to be 400 ± 170 nm, approximately three times greater than the roughness reported by Dixon et al. (2016). After deposition of the dielectric and hydrophobic films, roughness on IJPs was 189 ± 12 nm and roughness on CRFs was approximately equal to the resolution of the profilometer (73 ± 7 nm). The increased roughness on IJPs could indicate increased defect density on the upper surface of the polymer layer. Kozbial et al. defined defect density as surface quality or the density of local step edges and point defects. They found that it was associated with decreased initial contact angles and increased surface heterogeneity (Kozbial et al. 2017). Increased heterogeneity is also associated with increased variability in the measurement of static contact angles and contact angle hysteresis (Li and Neumann 1992; Raj et al. 2012; Kozbial et al. 2017).

Increased roughness of the IJP electrodes could also increase apparent heterogeneity of the device under an applied voltage due to variations in the local electrowetting number (Fig. 4a, b). If roughness of the conductive layer was significant relative to dielectric layer thickness, local Ew would increase above areas with thinner dielectric layers, and decrease above areas with thicker dielectric layers (Fig. 4c). Appreciable differences in dielectric layer thickness would be expected to increase apparent heterogeneity at low-to-moderate voltages, but heterogeneity would be expected to decrease at large voltages as local apparent contact angles become saturated (Fig. 4d).

Electrowetting performance on both IJPs and CRFs was initially well predicted by the Lippmann–Young equation.

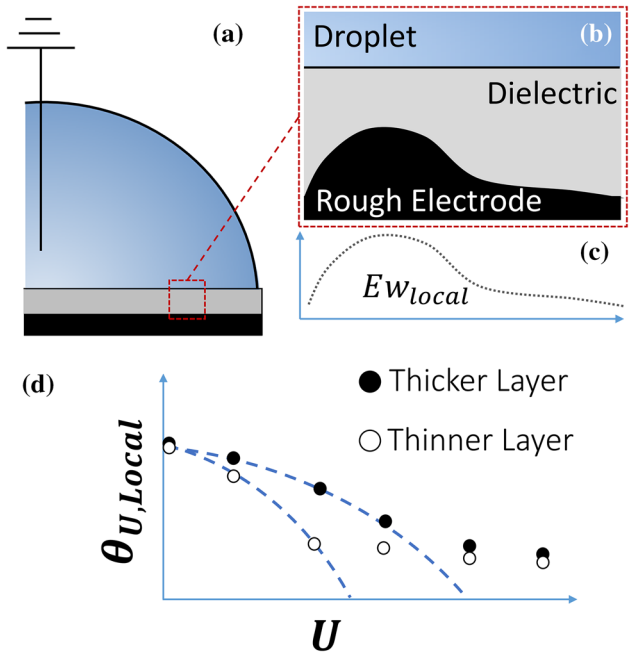

Fig. 4 Side-view sketches of **a** a DMF device, **b** an exploded view showing a difference in electrode roughness (not to scale), and expected effects of differences in local dielectric layer thickness on **c** electrowetting number and **d** electrowetting performance

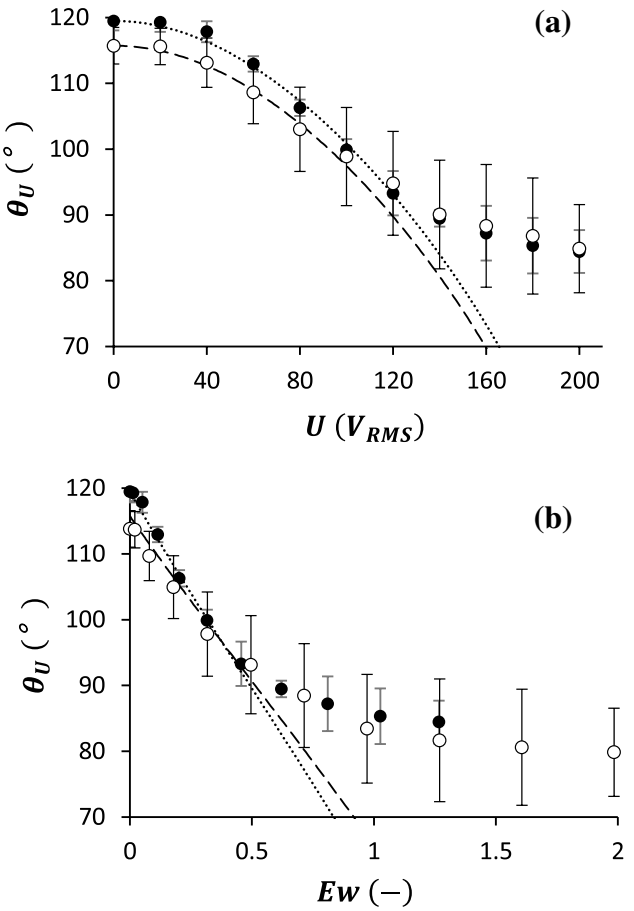

Fig. 5 Experimentally observed contact angles on inkjet-printed (open) and cleanroom-fabricated (closed) devices as a function of **a** RMS voltage and **b** electrowetting number. Dashed and dotted lines show predictions from the Young–Lippmann equation for IJP and CRF devices, respectively

Deviation from the prediction occurs at similar voltages and Ew on IJPs ($U \approx 120$ V_{RMS}, Ew ≈ 0.50) and CRFs ($U \approx 140$ V_{RMS}, Ew ≈ 0.62) and full saturation occurred at approximately Ew ≈ 1.0 on both device types (Fig. 5). The difference in the performance of these devices was mainly the result of differences in dielectric layer thicknesses and initial contact angles. The thicker dielectric layer on the CRFs causes a more rapid decrease in apparent contact angle with applied voltage or electrowetting number. But since initial contact angle on IJPs (115.7°) was lower than on CRFs (118.5°), the apparent contact angle on IJPs was lower at all applied voltages before the onset of saturation. While the initial contact angle was slightly lower on IJP devices, the difference between device types seen here was similar to the uncertainty in the measurement and not significantly different than the variation in initial contact angle observed across multiple experiments on CRF devices (Li and Mugele 2008). This suggests that the increased roughness on IJPs did not have a significant impact on the initial contact angle.

Measurement uncertainty on both device types initially increased with Ew. This is consistent with observations by Li and Mugele (2008). Uncertainty on IJPs increased more rapidly than on CRFs for low-to-moderate electrowetting numbers (Ew < 0.65). The difference in uncertainty between device types began to decrease above Ew ≈ 0.65until they were comparable at Ew ≈ 1.0 (Fig. S1a). Increased uncertainty in static contact angles on IJPs is consistent with the hypothesis that roughness of the printed electrodes increases the heterogeneity of the surface of the device by increasing the density of surface defects. The evolution in uncertainty with Ew is consistent with the hypothesis that electrowetting on rough electrodes can alter the apparent heterogeneity of the device. The apparent heterogeneity of the devices could likely be reduced by increasing dielectric layer thickness, but this would come at the cost of requiring higher actuation voltage to achieve a given electrowetting number.

The similarity in the apparent contact angles and electrowetting performance of CRFs and IJPs does not ensure similarity of contact angle hysteresis on both device types (Burkhart et al. 2017). Contact angle hysteresis is an important parameter for applications involving colloidal deposition in evaporating droplets because depinning of the contact line can dramatically change the flow in an evaporating droplet (Masoud and Felske 2009; Larson 2014; Burkhart et al. 2017). High hysteresis may also dampen the

electrowetting response and prevent electrowetting-assisted droplet detachment.

Despite differences in the electrowetting performance, contact angle hysteresis on IJPs and CRFs agreed to within $0.2° \pm 3.0°$ across all electrowetting numbers examined here (Fig. 6). As predicted by Li and Mugele (2008), contact angle hysteresis under AC actuation decreased with increasing electrowetting number on both device types. Although IJPs and CRFs have similar average contact angle hysteresis, measurement uncertainty was generally higher on IJPs ($\pm 2.6°$) than CRFs ($\pm 1.6°$). The difference between the uncertainty on these device types again increases with Ew at low-to-moderate Ew and decreases as the devices experience contact angle saturation (Fig. S1b). This behavior is consistent with the hypothesis that increased roughness of the printed electrodes increases heterogeneity on the surface of the device by increasing defect density and/or the variation in the local electrowetting number.

The advancing and receding contact angles can be used to quantify the total contact line pinning force as a function of Ew on both device types. As shown by Li and Mugele, the total pinning force per unit length along the contact line (δF_{tot}) at a given Ew can be described as:

$$\delta F_{\text{tot}}(\text{Ew}) = \delta F_R(\text{Ew}) + \delta F_A(\text{Ew}) = \gamma\left[\cos\left(\theta_{R,\text{Ew}}\right) - \cos\left(\theta_{A,\text{Ew}}\right)\right], \quad (2)$$

where δF_A and δF_R are the pinning forces per unit length in the advancing and receding directions, γ is the surface tension between the fluid and the surrounding medium, and $\theta_{R,\text{Ew}}$ and $\theta_{A,\text{Ew}}$ are the receding and advancing contact angles observed at a given electrowetting number (Li and Mugele 2008). Scaling δF_{tot} by surface tension yields

$$\delta F^*_{\text{tot,Ew}} = \left(\delta F_{\text{tot}}/\gamma\right) = \cos\left(\theta_{R,\text{Ew}}\right) - \cos\left(\theta_{A,\text{Ew}}\right). \quad (3)$$

This dimensionless total contact line pinning force per unit length ($\delta F^*_{\text{tot,Ew}}$) decreased with electrowetting number on IJPs and CRFs, and results were generally in good agreement on both device types (Fig. 7). These results also generally agree with experimental and analytical results presented by Li and Mugele that suggest that $\delta F^*_{\text{tot,Ew}}$ under AC electrowetting decreases linearly from Ew = 0 to Ew = $\left[\cos\left(\theta_{R,\text{Ew=0}}\right) - \cos\left(\theta_{A,\text{Ew=0}}\right)\right]/2$ and remains consistent thereafter (Li and Mugele 2008).

Since the pinning force is derived from advancing and receding contact angle data, it is not surprising that experimental uncertainty was again higher on IJP devices at low-to-moderate Ew and similar as the device approaches contact angle saturation (Fig. S1c). This repeated trend suggests that the low-cost fabrication of IJPs comes with increased variability as seen by the increased size of the error bars in all IJP results. This increased uncertainty is consistent with an increase in heterogeneity on the hydrophobic surface due to increased roughness of the IJP electrodes. Further study is required to confirm this mechanism.

Surface adhesion on IJPs and CRFs was examined by performing electrowetting-induced droplet detachment as described by Lee et al. (2014). This investigation provides what the authors believe is the first demonstration of electrowetting-induced droplet detachment on IJPs.

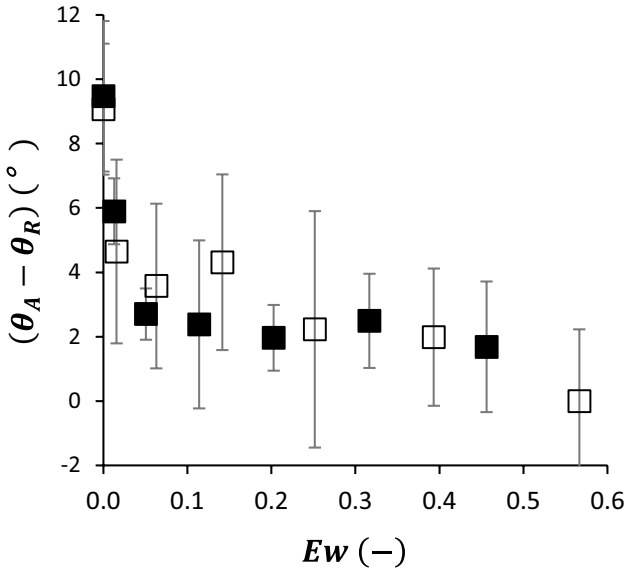

Fig. 6 Contact angle hysteresis ($\theta_A - \theta_R$) as a function of electrowetting number for inkjet-printed (open) and cleanroom-fabricated (closed) devices

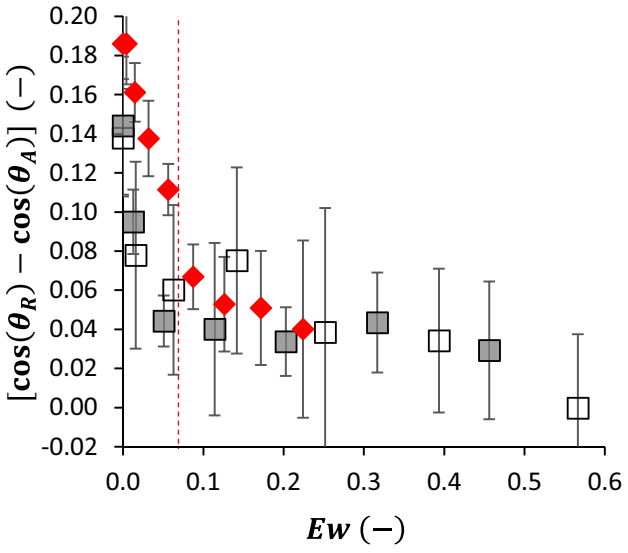

Fig. 7 Evolution of δF^*_{tot} as a function of Ew on inkjet-printed (open square) and cleanroom-fabricated devices (closed square). Data from Li and Mugele (closed circle) is also shown [57]. δF^*_{tot} is expected to decrease linearly until Ew = $\left[\cos\left(\theta_{R,0}\right) - \cos\left(\theta_{A,0}\right)\right]/2$ (dashed line)

When an actuation pulse on a droplet is tuned to the wetting time, the droplet can overcome surface adhesion and fully detach from the surface. Adhesion work (W_{adh}) can be estimated as:

$$W_{adh} \approx \gamma\left[1 + \cos\left(\theta_0\right)\right], \tag{4}$$

where θ_0 is the unactuated initial contact angle between the droplet and the device and γ is the surface tension between the droplet and the surrounding medium. It has been demonstrated that the electrical energy in the system ($\gamma \cdot \mathrm{Ew}$) must be greater than the adhesion work for the droplet to detach from the surface (Lee et al. 2014). By equating the electrical energy to the work of adhesion, a minimum threshold electrowetting number (Ew_{min}) for detachment can be predicted as

$$\mathrm{Ew}_{min} = 1 + \cos\left(\theta_0\right). \tag{5}$$

The lower initial unactuated contact angle on IJPs suggests that the adhesion work on IJPs is greater than that on CRFs. This leads to a higher predicted Ew_{min} for IJPs (0.57) than CRFs (0.51).

Experimentally observed Ew_{min}values agreed well with theoretical predictions on both IJPs (Ew ≈ 0.60) and CRFs (Ew ≈ 0.48) (Fig. 8). As expected, the increased adhesion energy on IJPs required the addition of more electrical energy at the solid–liquid interface than CRFs. Complete detachment was possible on all IJP devices despite an increase in adhesion work of approximately 25%. This may not have been the case if an increase in hysteresis on the IJPs was large enough to dampen the contact line dynamics of the droplet or if the reduction in the unactuated contact angle increased Ew_{min} beyond the threshold for contact angle saturation.

The frame rate used in this investigation (40 fps) was well below the 5000 fps used by Lee et al. (2014) to characterize the dynamics and maximum height of electrowetting-induced droplet detachment. However, results presented here suggest that the wetting dynamics are similar on CRFs and IJPs. Electrowetting-induced droplet detachment requires that the duration of the actuation pulse be tuned to the wetting dynamics so the electrical signal is removed after the contact line overshoots its final position but before it reaches steady state. Since full detachment was observed at the predicted electrowetting number on both devices using the same actuation signal, wetting dynamics on these devices are likely similar. This may not have been the case if the contact angle hysteresis on the IJPs was significantly greater than that on CRFs.

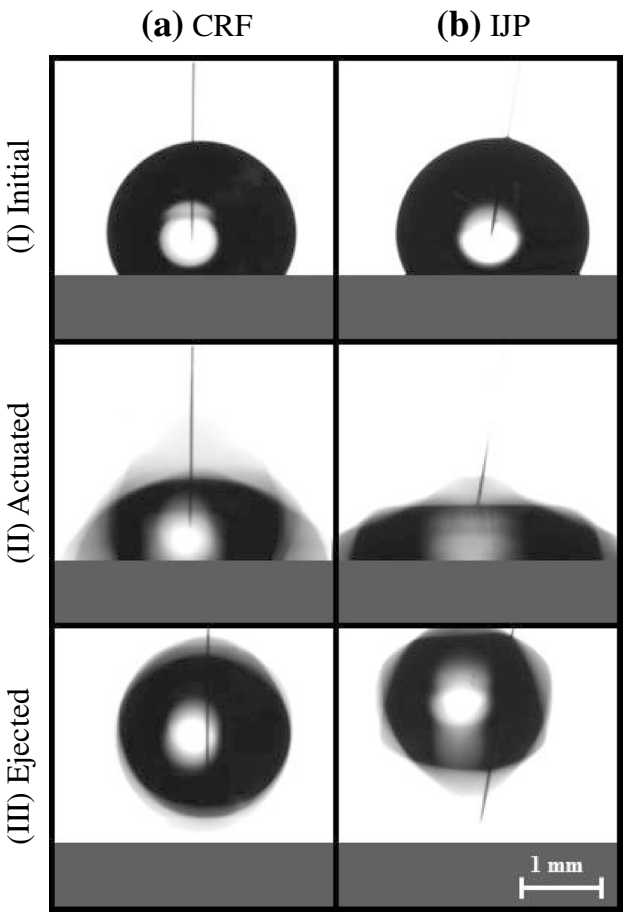

Fig. 8 Typical experimental images of complete electrowetting-induced droplet detachment from (**a**) cleanroom-fabricated and (**b**) inkjet-printed devices. Images represent (I) initial, (II) actuated, and (III) ejected droplets

4 Conclusions

Experimental results presented here suggest that digital microfluidic devices with low-cost inkjet-printed electrodes are suitable for investigations examining colloidal transport and deposition in evaporating droplets under electric fields, and electrowetting-induced droplet detachment. Such examinations have a wide range of applications in biomedical technology, flexible electronics fabrication, photonics, nanoparticle self-assembly, and active shedding of droplets from a variety of surfaces.

This investigation characterizes electrowetting performance, contact angle hysteresis, contact line pinning force, and adhesion work at the solid–liquid interface of digital microfluidic devices with inkjet-printed and cleanroom-fabricated electrodes. Average performance across all parameters of interest was similar on both device types. Differences in electrowetting performance were due to thinner dielectric layers and lower initial contact angles on inkjet-printed devices. The contact angle hysteresis and pinning forces along the contact line were comparable over a range of electrowetting numbers and agreed well with previously published work on other cleanroom-fabricated devices. While the average performance for these parameters was similar

on both device types, the low-cost inkjet-printed devices exhibited greater variability in performance, particularly at low-to-moderate electrowetting numbers. While these results are consistent with the hypothesis that increased roughness of the inkjet-printed electrodes increases heterogeneity on the hydrophobic surface of the device by increasing the density of surface defects and/or increasing the variation in the local value of the electrowetting number, further study is required to confirm these mechanisms. This suggests that use of inkjet-printed electrodes in digital microfluidic investigations should be accompanied with a rigorous uncertainty analysis.

This work also demonstrates that analytical predictions of the critical electrowetting number are valid for both inkjet-printed and cleanroom-fabricated devices. While adhesion work at the interface between the droplet and the surface was approximately 25% greater on devices with inkjet-printed electrodes, full droplet detachment was observed on both device types. This may not have been the case if increased hysteresis on the inkjet-printed devices dampened the contact line dynamics of the droplet or if increased adhesion energy pushed the critical electrowetting number for droplet detachment above the value for contact angle saturation.

Acknowledgements The authors gratefully acknowledge the assistance of Hee Tae An and the SMFL at RIT for sputter deposition of material on cleanroom-fabricated devices, Cammie Johanning for printer selection and contributions to the experimental methodology, and Anna Tilstra-Smith and Dhanya Thiyagarajan for assisting with printer repair and preliminary data collection. We also thank Dr. Denis Cormier, Dr. Bruce Kahn, and Manoj Meda at the RIT AMPrint center for assistance with the resistivity testing, PulseForge sintering, and roughness measurements.

Funding This material is based upon work supported by the ADVANCE RIT grant which is funded through the National Science Foundation under Award No. HRD-1209115. The authors also gratefully acknowledge the financial support of the Kate Gleason College of Engineering.

References

Abdelgawad M, Wheeler AR (2007) Low-cost, rapid-prototyping of digital microfluidics devices. Microfluid Nanofluidics 4:349–355. https://doi.org/10.1007/s10404-007-0190-3

Bellido E, Ojea-Jiménez I, Ghirri A et al (2012) Controlled positioning of nanoparticles on graphene by noninvasive AFM lithography. Langmuir 28:12400–12409. https://doi.org/10.1021/la3023419

Bromberg V, Ma S, Egitto FD, Singler TJ (2013a) Highly conductive lines by plasma-induced conversion of inkjet-printed silver nitrate traces. J Mater Chem C 1:6842. https://doi.org/10.1039/c3tc31361a

Bromberg V, Ma S, Singler TJ (2013b) High-resolution inkjet printing of electrically conducting lines of silver nanoparticles by edge-enhanced twin-line deposition. Appl Phys Lett 102:214101. https://doi.org/10.1063/1.4807782

Burkhart CT, Maki KL, Schertzer MJ (2017) Effects of interface velocity, diffusion rate, and radial velocity on colloidal deposition patterns left by evaporating droplets. ASME J Heat Transf 139:111501–111505. https://doi.org/10.1115/1.4036681

Cavalli A, Preston DJ, Tio E et al (2016) Electrically induced drop detachment and ejection. Phys Fluids. https://doi.org/10.1063/1.4940213

Chae JB, Lee SJ, Yang J, Chung SK (2015) 3D electrowetting-on-dielectric actuation. Sens Actuators A Phys 234:331–338. https://doi.org/10.1016/j.sna.2015.09.004

Chen Y, Müller JD, So PT, Gratton E (1999) The photon counting histogram in fluorescence fluctuation spectroscopy. Biophys J 77:553–567. https://doi.org/10.1016/S0006-3495(99)76912-2

Cho SK, Moon H, Kim C-J (2003) Creating, transporting, cutting, and merging liquid droplets by electrowetting-based actuation for digital microfluidic circuits. J Microelectromech Syst 12:70–80

Choi K, Ng AHC, Fobel R, Wheeler AR (2012) Digital microfluidics. Annu Rev Anal Chem (Palo Alto Calif) 5:413–440. https://doi.org/10.1146/annurev-anchem-062011-143028

Corkidi G, Montoya F, Cruz GH, Vargas M (2016) Evaporation dynamics and sedimentation pattern of a sessile particle laden water droplet. Exp Fluids 57:1–11. https://doi.org/10.1007/s00348-016-2182-0

Dixon C, Ng AHC, Fobel R et al (2016) An inkjet printed, roll-coated digital microfluidic device for inexpensive, miniaturized diagnostic assays. Lab Chip 16:4560–4568. https://doi.org/10.1039/C6LC01064D

Eral HB, Augustine DM, Duits MHG, Mugele F (2011) Suppressing the coffee stain effect: how to control colloidal self-assembly in evaporating drops using electrowetting. Soft Matter 7:4954. https://doi.org/10.1039/c1sm05183k

Fobel R, Kirby AE, Ng AHC et al (2014) Paper microfluidics goes digital. Adv Mater 26:2838–2843. https://doi.org/10.1002/adma.201305168

Gulka CP, Swartz JD, Trantum JR et al (2014) Coffee rings as low-resource diagnostics: detection of the malaria biomarker Plasmodium falciparum histidine-rich protein-II using a surface-coupled ring of Ni(II)NTA gold-plated polystyrene particles. ACS Appl Mater Interfaces 6:6257–6263. https://doi.org/10.1021/am501452k

Hayes RA, Feenstra BJ (2003) Video-speed electronic paper based on electrowetting. Nature 425:383–385

Hong J, Kim YK, Kang KH et al (2013) Effects of drop size and viscosity on spreading dynamics in DC electrowetting. Langmuir 29:9118–9125. https://doi.org/10.1021/la401801u

Hong J, Kim YK, Won D-J et al (2015) Three-dimensional digital microfluidic manipulation of droplets in oil medium. Sci Rep 5:10685. https://doi.org/10.1038/srep10685

Ikawa M, Yamada T, Matsui H et al (2012) Simple push coating of polymer thin-film transistors. Nat Commun 3:1–8. https://doi.org/10.1038/ncomms2190

Kim HY (2004) Drop fall-off from the vibrating ceiling. Phys Fluids 16:474–477. https://doi.org/10.1063/1.1637352

Kim J, Kaviany M (2007) Purging of dropwise condensate by electrowetting. J Appl Phys. https://doi.org/10.1063/1.2734933

Kim J, Kaviany M (2010) Electrowetting purged surface condensate in evaporators. Heat Transf Eng 31:101–107. https://doi.org/10.1080/01457630903285302

Klarman D, Andelman D, Urbakh M (2011) A model of electrowetting, reversed electrowetting, and contact angle saturation. Langmuir 27:6031–6041. https://doi.org/10.1021/la2004326

Ko H, Lee J, Kim Y et al (2014) Active digital microfluidic paper chips with inkjet-printed patterned electrodes. Adv Mater 26:2335–2340. https://doi.org/10.1002/adma.201305014

Kong M, Chen D, Chen X et al (2017) Research of the human eye model with variable—focus liquid lens. Microfluid Nanofluidics 21:1–5. https://doi.org/10.1007/s10404-017-1857-z

Kozbial A, Trouba C, Liu H, Li L (2017) Characterization of the intrinsic water wettability of graphite using contact angle measurements: effect of defects on static and dynamic contact angles. Langmuir 33:959–967. https://doi.org/10.1021/acs.langmuir.6b04193

Kuiper S, Hendriks BHW (2004) Variable-focus liquid lens for miniature cameras variable-focus liquid lens for miniature cameras. Appl Phys Lett 85:1128–1130. https://doi.org/10.1063/1.1779954

Larson RG (2014) Transport and deposition patterns in drying sessile droplets. AIChE J 60:1538–1571. https://doi.org/10.1002/aic

Layani M, Gruchko M, Milo O et al (2009) Transparent conductive coatings by printing coffee ring arrays obtained at room temperature. ACS Nano 3:3537–3542. https://doi.org/10.1021/nn901239z

Lee SJ, Lee S, Kang KH (2012) Droplet jumping by electrowetting and its application to the three-dimensional digital microfluidics. Appl Phys Lett. https://doi.org/10.1063/1.3688487

Lee SJ, Hong J, Kang KH et al (2014) Electrowetting-induced droplet detachment from hydrophobic surfaces. Langmuir 30:1805–1811. https://doi.org/10.1021/la404344y

Li F, Mugele F (2008) How to make sticky surfaces slippery: contact angle hysteresis in electrowetting with alternating voltage. Appl Phys Lett 92:12–15. https://doi.org/10.1063/1.2945803

Li D, Neumann AW (1992) Surface heterogeneity and contact angle hysteresis. Colloid Polym Sci 270:498–504

Li Y, Mckenna EO, Parkes W et al (2011) The application of fixed hydrophobic patterns for confinement of aqueous solutions in proteomic microarrays. Appl Phys Lett 99:1–3. https://doi.org/10.1063/1.3626037

Mampallil D, Eral HB, van den Ende D, Mugele F (2012) Control of evaporating complex fluids through electrowetting. Soft Matter 8:10614. https://doi.org/10.1039/c2sm26103k

Mannetje TDJCM, Murade CU, Van Den Ende D, Mugele F (2011) Electrically assisted drop sliding on inclined planes. Appl Phys Lett. https://doi.org/10.1063/1.3533362

Masoud H, Felske JD (2009) Analytical solution for stokes flow inside an evaporating sessile drop: spherical and cylindrical cap shapes. Phys Fluids 21:1–11. https://doi.org/10.1063/1.3112002

McHale G (2007) Surface free energy and microarray deposition technology. Analyst 132:192–195. https://doi.org/10.1039/b617339j

Mu J, Lin P, Xia Q (2014) Concentric rings of polystyrene and titanium dioxide nanoparticles patterned by alternating current signal guided coffee ring effect. Appl Phys Lett. https://doi.org/10.1063/1.4886138

Mugele F (2009) Fundamental challenges in electrowetting: from equilibrium shapes to contact angle saturation and drop dynamics. Soft Matter 5:3377. https://doi.org/10.1039/b904493k

Mugele F, Baret J-C (2005) Electrowetting: from basics to applications. J Phys Condens Matter 17:R705–R774. https://doi.org/10.1088/0953-8984/17/28/R01

Nelson WC, Kim C-J (2012) Droplet actuation by electrowetting-on-dielectric (EWOD): a review. J Adhes Sci Technol 26:1747–1771. https://doi.org/10.1163/156856111X599562

Ng AHC, Fobel R, Fobel C et al (2018) A digital microfluidic system for serological immunoassays in remote settings. Sci Transl Med 10:1–13

Orejon D, Sefiane K, Shanahan MER (2011) Stick-slip of evaporating droplets: substrate hydrophobicity and nanoparticle concentration. Langmuir 27:12834–12843. https://doi.org/10.1021/la2026736

Orejon D, Sefiane K, Shanahan MER (2013) Evaporation of nanofluid droplets with applied DC potential. J Colloid Interface Sci 407:29–38. https://doi.org/10.1016/j.jcis.2013.05.079

Paik P, Pamula VK, Pollack MG, Fair RB (2003) Electrowetting-based droplet mixers for microfluidic systems. Lab Chip 3:28–33. https://doi.org/10.1039/b210825a

Palan V, Shepard WS (2006) Enhanced water removal in a fuel cell stack by droplet atomization using structural and acoustic excitation. J Power Sources 159:1061–1070. https://doi.org/10.1016/j.jpowsour.2005.12.020

Rackus DG, Campos RPS, De Chan C et al (2017) Pre-concentration by liquid intake by paper (P-CLIP): a new technique for large volumes and digital microfluidics. Lab Chip 17:2272–2280. https://doi.org/10.1039/C7LC00440K

Ragoonanan V, Aksan A (2008) Heterogeneity in desiccated solutions: implications for biostabilization. Biophys J 94:2212–2227. https://doi.org/10.1529/biophysj.107.110684

Raj R, Enright R, Zhu Y et al (2012) Unified model for contact angle hysteresis on heterogeneous and superhydrophobic surfaces. Langmuir 28:15777–15788. https://doi.org/10.1021/la303070s

Roghair I, Musterd M, Ende D, Van Den Kleijn C (2015) A numerical technique to simulate display pixels based on electrowetting. Microfluid Nanofluidics. https://doi.org/10.1007/s10404-015-1581-5

Saha A, Basu S, Kumar R (2012) Particle image velocimetry and infrared thermography in a levitated droplet with nanosilica suspensions. Exp Fluids 52:795–807. https://doi.org/10.1007/s00348-011-1114-2

Samiei E, Luka GS, Najjaran H, Hoorfar M (2016) Integration of biosensors into digital microfluidics: impact of hydrophilic surface of biosensors on droplet manipulation. Biosens Bioelectron 81:480–486. https://doi.org/10.1016/j.bios.2016.03.035

Schertzer MJ, Gubarenko SI, Ben-Mrad R, Sullivan PE (2010) An empirically validated analytical model of droplet dynamics in electrowetting on dielectric devices. Langmuir 26:19230–19238

Schertzer MJ, Ben Mrad R, Sullivan PE (2012) Automated detection of particle concentration and chemical reactions in EWOD devices. Sensors Actuators B Chem 164:1–6. https://doi.org/10.1016/j.snb.2012.01.027

Torabinia M, Farzbod A, Moon H et al (2018) Electromechanical model to predict the movability of liquids in an electrowetting-on-dielectric microfluidic device. J Appl Phys. https://doi.org/10.1063/1.5014045

Trantum JR, Wright DW, Haselton FR (2012) Biomarker-mediated disruption of coffee-ring formation as a low resource diagnostic indicator. Langmuir 28:2187–2193. https://doi.org/10.1021/la203903a

Walker S, Shapiro B (2006) Modeling the fluid dynamics of electrowetting on dielectric (EWOD). J Microelectromech Syst 15:986

Wang H, Chen L, Sun L (2017) Digital microfluidics: a promising technique for biochemical applications. Front Mech Eng 12:510–525. https://doi.org/10.1007/s11465-017-0460-z

Wang Y, Ruan Q, Lei Z et al (2018) Highly sensitive and automated surface enhanced raman scattering-based immunoassay for H5N1 detection with digital microfluidics. Anal Chem 90:5224–5231. https://doi.org/10.1021/acs.analchem.8b00002

Watson MWL, Abdelgawad M, Ye G et al (2006) Microcontact printing-based fabrication of digital microfluidic devices. Anal Chem 78:7877–7885. https://doi.org/10.1021/ac0613378

Wen JT, Ho CM, Lillehoj PB (2013) Coffee ring aptasensor for rapid protein detection. Langmuir 29:8440–8446. https://doi.org/10.1021/la400224a

Yung KC, Gu X, Lee CP, Choy HS (2010) Ink-jet printing and camera flash sintering of silver tracks on different substrates. J Mater Process Technol 210:2268–2272. https://doi.org/10.1016/j.jmatprotec.2010.08.014

Zhang H, Yan Q, Xu Q et al (2017) A sacrificial layer strategy for photolithography on highly hydrophobic surface and its application for electrowetting devices. Sci Rep. https://doi.org/10.1038/s41598-017-04342-z